Negative ion resonance measurements in the autoionising region of helium measured across the complete angular scattering range (0°-180°).

R Ward[1,5] , D Cubric[2], N Bowring[3], G C King[2], F H Read[2], D V Fursa[4], I Bray[4].

[1] School of Computing and Engineering, University of Huddersfield, Queensgate, Huddersfield, HD1 3DH, UK.

[2] School of Physics and Astronomy, Schuster Laboratory, Manchester University, Manchester M13 9PL, UK.

[3] Faculty of Science & Engineering, John Dalton Building, Chester Street, Manchester, M1 5GD, UK.

[4]ARC Centre for Antimatter-Matter Studies, Curtin University of Technology, GPO Box U1987 Perth, Western Australia 6845, Australia.

Abstract

Excitation function measurements for the decay of the $2s^2 2p\ ^2P$ and $2s2p^2\ ^2D$ triply excited negative ion resonances in helium to singly excited n=2 states have been measured. These excitation functions have been determined across the complete angular range (0-180°) using a magnetic angle changer (MAC) with a soft-iron core. The convergent close-coupling method has been used to calculate the cross sections, with the underlying complexity of the problem not yet being able to be fully resolved. Agreement between the present experimental data and previous experimental data is good, with these excitation functions confirming the presence of an unusual $(2s^2 2p)^2P$ resonance behaviour in the 2^1S channel at 90°, where this would not usually be expected. Resonance energy and width values have been obtained, with a mean energy for the $(2s^2 2p)^2P$ resonance of 57.20 ± 0.08 eV and a mean width of 73 ± 20 meV, and a mean energy of the $(2s2p^2)^2D$ resonance of 58.30 ± 0.08 eV and a mean width of 59 ± 27 meV. Resonant cross section

[5] Corresponding Author, e-mail: rupert.ward@hud.ac.uk

and ρ^2 values have been calculated across the angular range for the first time, providing angular distribution data on decay propensities for both resonances.

PACS numbers:
34.80.Dp Atomic excitation and ionisation
34.10.+x General theories and models of atomic and molecular collisions and interactions (including statistical theories, transition state, stochastic and trajectory models, etc.)

1. Introduction

Negative ion resonances, also known as compound states or temporary negative ions, have been investigated both theoretically and experimentally, for almost 50 years [1]. Both the resonances themselves, and the electron correlations which govern their behaviour, are important factors in a broad range of fields, including superconductivity [2] and plasma physics [3], properties of graphene [4], fullerene [5], carbon nanotubes [6] and polymers [7], atmospheric physics [8], astrophysics [9] and as part of interactions involving proteins and DNA [10].

The theoretical challenges of modelling negative ion resonances are significant due to the sensitivity of such states to the effects of electron correlation [11] and therefore progress in this area is of general benefit both to the fields outlined above, and in understanding the characteristics of atomic systems and how they interact. Helium provides the prototypical example both of triply excited negative ion resonances and more broadly of weakly bound multi-electron resonances in general. Studies of helium both experimentally and theoretically enable models to be tested and intrinsic properties of general behaviour to be identified. Multi-electron negative ion resonances present a particular challenge to theoretical and computational modelling as the Coulomb attraction is weaker than in neutral or positive ion resonances (compared with the inter-electronic repulsion) and so a clear solution based on Hartree-Fock or Multi-Configurational Hartree Fock calculations is both less likely, and where possible, less well defined [12]. Specifically to the present study, the theoretical challenge is quite substantial due to the conflicting nature of the ground state, which requires short-ranged correlations, and the autoionizing states, which require long-ranged functions for their accurate description. As part of this work we show that this remains an as yet unresolved challenge, at least for the convergent close-coupling theory [13].

The theoretical principles governing negative ion resonance formation were developed primarily from the work of Fano [14,15]. The key reviews of progress in this field by Schulz in 1973 [16] and Buckman and Clark in 1994 [17] identify several theoretical concepts which are of relevance to this paper, namely: the determination of type 1 and type 2 resonances [18,19]; the evaluation of q values from experiments [20]; a reformulation of the Fano profiles into a more convenient parameterisation [21]; and the treatment of broadened profiles [22,].

Experimentally triply excited negative ion states were first observed by Kuyatt et al. in 1965 [23] and classified by Fano and Cooper the same year [15]. Further theoretical and experimental results have been published since by Burrow and Schulz [24], Grissom et al. [25], Eliezer and Pan [26], Golden and Zecca [27], Quéméner [28], Nicolaides [29], Sanche and Schulz [30], Marchand [31], Ahmed [32], Smith [33], Hicks [34], Nesbet [35], Roy [36], Gosselin [37], Bylicki [38], Bylicki and Nicolaides [39] and Trantham et al. [40]. These results are presented in Table 1 to Table 3 and discussed in comparison with the current work in the results and discussion section.

Historically studies of negative ion resonances in the autoionising region of helium have provided debate and disagreement both on the existence of resonances and on their configurations [17,41,42,43], with the presence of nearby autoionising states and potential Post-Collision Interaction (PCI) effects making accurate identification and assignment of states in this energy range complex. General agreement has been reached on the resonance energies of the two lowest-lying triply excited negative ion resonance states at 57.2eV and 58.3eV [23], and Trantham et al. [40] proposed their classifications as $(2s^2 2p)^2P$ and $(2s2p^2)^2D$ respectively. Trantham et al. discussed the structure of these highly correlated states, investigating configurations proposed in the earlier work of Morishita and Lin [44], who had reviewed these resonance states from a theoretical perspective and suggested three different possible configurations for these resonances.

This aim of this work therefore is to confirm the correct structures for these contested resonances by comparing the current experimental results to the work of Trantham et al. [40] and by considering the theoretical configurations proposed by Morishita and Lin [44]. The work also provides an opportunity to check for the unusual resonance behaviour seen in the previous experimental work by Trantham et al., and where possible to theoretically model these resonances. Finally the work provides both resonance cross-section and resonant ratio data for these resonance states across the full angular range for the first time, including a limited comparison with the CCC theory.

2. Resonance Theory

The Fano profile [14] (see Equation 1) is based on the interference between discrete and continuous wavefunctions. In the present work on negative ions the two interfering processes are the direct excitation of the n = 2 singly excited states of helium and their excitation via decay of a negative ion.

The Fano profile has been used in several forms by different authors [21,22]. In the current work the formulation by Shore, also known as the Shore Profile, has been adopted (see Equation 2).

$$\sigma(E,\theta) = \sigma_a \cdot \frac{(q+\varepsilon)^2}{1+\varepsilon^2} + \sigma_b \tag{1}$$

$$\sigma(E,\theta) = C(E) + \frac{B\left(\frac{\Gamma}{2}\right) + A\left(E - E_0\right)}{\left(E - E_0\right)^2 + \left(\frac{\Gamma}{2}\right)^2} \tag{2}$$

$$\frac{B}{A} = \frac{q^2 - 1}{2q} \tag{3}$$

$$\rho^2 = \frac{\sigma_a}{\sigma_a + \sigma_b} \tag{4}$$

$$\varepsilon = \frac{2(E - E_0)}{\Gamma} \tag{5}$$

In Equation 1 $\sigma(E,\theta)$ is the cross section profile, σ_a is the resonant cross section, σ_b is the background cross section, q is the line shape parameter and ε is the scaled energy departure from resonance. In Equation 2 again $\sigma(E,\theta)$ is the cross section profile, C(E) is the background signal, B and A are the symmetric and asymmetric components of the line shape, Γ is the width of the state and E_0 is the resonance energy. The line shape parameter q in Equation 1 is related to B and A in Equation 2 via Equation 3. The overlap integral of the states formed by direct and resonant transition from the ground state (ρ), is found via a ratio of the resonant cross section σ_a and the background cross section σ_b as shown in Equation 4. From Equations 1 and 2 it can also be shown that ε is simply the energy departure from resonance ($E-E_0$) scaled by the half-width ($\Gamma/2$) as shown in Equation 5.

The autoionising region of helium contains a number of doubly excited autoionising states and several negative ion states as shown in Table 1. One of the key issues in measuring negative ion resonances in this region is how to differentiate these from their neighbouring autoionising states. Appropriate decay channels must be chosen, based on the states that can be detected via these decay channels.

For higher orbital decay channels, Post-Collision Interaction (PCI), first identified by Hicks and colleagues in the early seventies [34], can mean it is difficult to differentiate between autoionising state decays and negative ion resonances. A Post-Collision Interaction occurs

when energy is exchanged, via a Coulomb interaction, between scattered and ejected electrons from the decay of an autoionising state. For this reason singly excited n=2 decay channels (2^3S, 2^1S, 2^3P, 2^1P), which are unlikely to have this difficulty [40], were chosen for this study. A further benefit of choosing these channels was their relatively high signal strengths, enabling sufficient data to be collected in a reasonable time.

The resonances present in the autoionising region themselves result from two slightly different interactions. Feshbach resonances occur when the kinetic energy of the incident electron is just below an excited state of the target atom, enabling the incident electron to be trapped in the resulting potential well. Shape resonances occur when the incident electron is trapped in the potential well resulting from the overlap of the attractive short range potential of the atom and the repulsive centrifugal potential. From Table 1 it can be seen for example that the states such as the 60.4eV state and those between 59.3 eV and 59.5 eV are extremely wide and therefore undetectable in the present study. Of the four remaining resonances, the 59.71 eV resonance is a narrow shape resonance decaying to the 58.31 eV autoionising state, and the 57.42 eV resonance would require either a spin or parity forbidden transition to be formed from the autoionising state and thus would appear weakly at best. The two remaining resonances, the $(2s^22p)^2P$ and $(2s2p^2)^2D$ states, which are narrow Feshbach resonances at approximately 57.2eV and 58.3eV respectively, therefore can be detected in the chosen decay channels without interference from other states.

In order to perform a direct comparison between the present experiment and theory, the latter must have both an accurate ground state and the autoionising states. The CCC theory relies on an orthogonal Laguerre basis for the generation of its target states [13]. To yield an accurate ground state, short-range 2s and 2p Laguerre orbitals are required with the same exponential fall-off as the $He^+(1s)$ orbital. However, the autoionising states require diffuse Laguerre orbitals for convergence. Without an accurate ground state energy the total energy in the system cannot match that of the experiment. Without accurate autoionising states the experimental structures cannot be definitively calculated. The compromise we choose, in order to have tractable calculations, is to work with a number of diffuse orbitals resulting in the existence of some of the autoionising states, but having a ground state energy in error by around 0.6 eV. This negates a quantitative comparison as the energy needs to be shifted and the results cannot be shown to be demonstrably convergent. Nevertheless a clear effect of the autoionising states on differential cross sections of excited states can be observed. More specifically, we constructed the helium states by first diagonalising the He+ Hamiltonian with 25-l Laguerre basis functions with the exponential fall off being four for l<=3, and then using the resulting orbitals to construct appropriately symmetrised configurations for diagonalising the He Hamiltonian. We keep all configurations that have the 1s, 2s, 2p, and 3p as the inner orbitals, and also 1snl configurations for the He excited states and the continuum. A total of 164 target states have been generated, and used to expand the total e-He wavefunction. The

close-coupling equations are formed in momentum space, and solved directly for the scattering amplitudes upon partial wave expansion [13], at every projectile energy considered.

3. Resonance configurations

Three resonance configurations have been postulated for the negative ion resonances under investigation. The first arrangement, proposed by Morishita and Lin [44], involves a doubly charged helium core surrounded by three electrons equidistant from the core and each other. This model uses a hyperspherical coordinate system with the energy differences between states resulting from rotational excitations. The lack of electron coupling in this arrangement leads to equal decay propensities for each electron. The two other possible arrangements involve a pair of coupled electrons. In the first of these, the coupled electrons are external to a singly charged core (doubly charged core plus inner electron), and the second consists of the reciprocal arrangement of a pair of coupled electrons close to the core orbited by a distant single electron, which experiences a weak attractive potential. The latter two arrangements preferentially decay to specific channels. The resonant structure for both the resonances under consideration can therefore be deduced by measuring decay propensities across the angular range.

The $(2s^2 2p)^2P$ resonance has two possible arrangements of electrons, $[2s(2s2p)^3P]^2P$ and $[2p(2s^2)^1S]^2P$. If $[2p(2s^2)^1S]^2P$ is correct the decay to 1s2p levels would result from one 2s electron decaying to 1s and the second 2s electron being ejected. The spin alignment of the remaining electrons (1s and 2p) is therefore arbitrary as the choice of which 2s electron is ejected is random. The decay to 1s2s levels is more complex. The decay can take place via two mechanisms: decay of one 2s electron and ejection of the 2p electron; or decay of the 2p electron to a 1s state and the transfer of one unit of angular momentum to a 2s electron which is then ejected as a p-wave electron. The latter dipole transition is less likely. The dominant monopole transition leaves the two s electrons which were previously coupled, and as these have opposite spin due to the exclusion principle the monopole transition will result in purely 2^1S states, with the 2^3S state only arising from the dipole transition i.e. the $[2p(2s^2)^1S]^2P$ structure is more likely to decay to a 2^1S state than 2^3S state.

A similar argument is used to analyse how the $[2s(2s2p)^3P]^2P$ structure decays. Here the 1s2p levels are populated evenly as the single 2s electron will decay with opposite spin compared to the p electron but the coupled electron will have its spin aligned. The 1s2s levels would favour the 2^3S state as the coupled dipole transition would result in aligned spins.

These arguments can be repeated for the $(2s2p^2)^2D$ resonance structures. It is found that the $[2p(2s2p)^3P]^2D$ structure results in the 2^3P decay being preferred over the 2^1P decay as the autodetachment of the single 2p electron results in aligned spins, and the 2^3S is favoured over the 2^1S for similar reasons. The $[2s(2p^2)^1S]^2D$ structure produces the opposite result with the singlet states preferred.

In summary an equidistant model will result in no difference in decay propensities, a resonance structure with coupled electrons of the same angular momentum will favour singlet state decays, and a resonance structure where coupled electrons have different angular momentum will favour triplet state decays.

Following simple angular momentum considerations, the $(2s^2 2p)^2P$ and $(2s2p^2)^2D$ resonances should also be absent from certain decay channels at certain angles, namely

- At 54º the $(2s2p^2)^2D$ resonance decay should be absent from the $2^{1,3}S$ channels
- At 90º the $(2s^2 2p)^2P$ resonance decay should be absent from the $2^{1,3}S$ channels
- At 90º the $(2s2p^2)^2D$ resonance decay should be absent from the $2^{1,3}P$ channels

Therefore by measuring at these angles and comparing decay propensities in the singlet and triplet channels of the allowed transitions, the structure of the negative ion resonances can be deduced. Further measurements at low and high angles provide additional insight into the behaviour of these resonances.

4. Apparatus and experimental procedures

Measurements of electron angular distributions in atomic and molecular physics have used various experimental configurations. A recent approach has been the adoption of the 'magnetic angle-changing technique' [45]. This technique produces a localized magnetic field, within the interaction region, thereby enabling controlled deflection of the electron trajectories. The first practical MAC devices, constructed at Manchester, were limited to low electron energies, below about 20 eV. This was due to the heat produced by the solenoid currents in the MAC and the need to dissipate this heat in an evacuated experimental chamber.

One solution to this problem, developed by Cubric et al. [46], is to incorporate a soft-iron core within the solenoids of the MAC. This significantly increases the magnetic field in the device, and hence greatly extends the range of electron energies that can be used. The present measurements involve higher electron energies, and hence the MAC described by Cubric et al [46] has been used. It is shown schematically in Figure 1. It uses two pairs of solenoids and appropriate currents flowing in opposite directions, so that the magnetic dipole moment of the MAC is zero. This, together with zero or minimal contributions from higher magnetic moments, ensures that the magnetic field has negligible effect on the operation of the electron spectrometer used in the measurements. The ferromagnetic material used for the MAC is soft iron with a magnetic permeability of approximately 1000. The magnetic hysteresis curve for soft iron is very narrow. Therefore it can be considered as a linear magnetic material, enabling currents to be applied without residual fields being generated within the angle changer.

The magnetic field produced by the MAC has been measured and the results are plotted in Figure 1 for a current of 1 A through the inner solenoids and a current of -0.772 A through the outer solenoids. As can be seen, the magnetic field is localized and changes its direction at a distance of about 12 mm from the central axis. Also shown in Figure 2 is the magnetic field variation from a comparable MAC without an iron core (which has been multiplied by a factor of 5). The magnetic field produced by the solenoids can also be calculated, using the following equation:

$$B_\rho(z,\rho,R,I)=\frac{\mu_0 I}{4\pi}\int_0^{2\pi}\frac{\rho z\cos(\phi)}{(\rho^2+z^2+R^2-2\rho R\cos(\phi))^{3/2}}d\phi, \qquad (6)$$

where R is solenoid radius and z and ρ are cylindrical polar coordinates representing respectively the axial and radial distances to the coil centre. The resulting magnetic field is due to the contributions from both solenoids. When a charged particle, of kinetic energy E, moves through a magnetic field B, it experiences a deflection proportional to B^2/E. Hence, by increasing the magnetic field by a factor of 5, using a soft-iron core, the device becomes capable of handling electron energies 25 times larger than the device without the iron core. The action of the MAC for inelastic electron scattering is illustrated in Figure 3. The

deflection from the MAC is proportional to energy and therefore the incident beam (originating from the right side, dashed line) is deflected slightly less than the scattered beam (solid line) whose residual energy is 20eV less. These beams are separated as they exit the MAC as can be seen at the bottom of Figure 3. The full angular range of the scattered beam can be detected as the solid lines exiting at 90° and 180° (relative to this straight through residual beam). The scattered beam can therefore be detected across the range of 0° - 180° by a traditional detector arrangement as the electron monochromator is always a significant distance from the electron energy analyser.

In the present work, the soft-iron core MAC has enabled the measurements at intermediate energies of approximately 60 eV where previous experimental data can be used for comparison purposes [40]. The MAC was used in conjunction with an electrostatic electron spectrometer consisting of an electron monochromator and an electron energy analyser, which could be rotated over the angular range from -10^{o} to 120^{o} with respect to the direction of the incident electron beam. The construction of the monochromator was based on a hemispherical selector having a mean radius of 50 mm. Two triple-aperture lenses were employed to focus the incident electron beam onto the target gas beam. A second set of two triple-aperture lenses was used to decelerate and focus scattered electrons from the target region onto the entrance aperture of a hemispherical electron analyser, again of 50 mm mean radius. Transmitted electrons were detected by a channel electron multiplier array. The incident electron beam current was monitored by a rotatable Faraday cup and typically had a value of 5 nA. The incident electron energy was calibrated against the position of the 2^2S resonance in helium (19.365 eV) and had an uncertainty of ± 115 meV, while the energy resolution of the present measurements was typically 130 meV (full width at half maximum). The angular resolution of the measurements (full width at half maximum) was estimated to be 6°. This value arose from the angular resolution of the spectrometer and the angular spread induced by the MAC. The target gas beam was produced by a single capillary of internal diameter of 0.5 mm and length 10 mm, and target pressures of typically 4.5×10^{-3} Pa were employed.

For the present measurements, the MAC was operated in the following way. In this procedure, care was taken to ensure that any background contributions were taken into account. These background contributions could arise from electrons scattering off residual gas in the experimental chamber or surfaces close to the interaction region. The decay channels 2^3S, 2^1S, 2^3P and 2^1P were scanned over the energy range 56 to 59 eV, with the duration of the scans varied from approximately 70 hours to 100 hours due to differences in signal strength. The detector was placed at 90º to the electron beam, with a current of ±0.29A applied to the solenoids of the magnetic angle changer to deflect the beam by 90º enabling a 180º scan with forward inelastic scattering separated from the incident beam. Data was obtained at 11 angles from 0º to 180º.

Once data was obtained, this was normalised against a known cross section, to calculate the differential cross section values. This technique has been used successfully previously to demonstrate independent agreement between a range of experimental and advanced theoretical models [47]. In this study the differential cross section of the 2^1P state was chosen as the reference using values obtained using the converging close-coupling method [48]. By comparing the theoretical curves for the 2^1P differential cross section with the measured electron intensities, the transmission of the electron energy analyser, as a function of scattering angle, could be determined for each value of incident electron energy. These transmission functions were then applied to the scattering data for the remaining states (2^3P, 2^1S, 2^3S) to obtain the differential cross sections. The resonant cross section measurements could then be calculated from these differential cross sections. All measurements were obtained under identical conditions of gas flow in the interaction region.

5. Results and discussion

For the sake of brevity the current measurements are only presented for the angles of 16°, 54º, 90º to compare with previous experimental results, at 90° to compare experiment with theory, and at 0º and 180º to demonstrate complete angular coverage. From the values obtained the energy and width of the resonances were calculated to be 57.20 ± 0.08 eV and 73 ± 20 meV for the $(2s^2 2p)^2P$ resonance, and 58.30 ± 0.08 eV and 59 ± 27 meV for the $(2s2p^2)^2D$ resonance.

5.1 Discussion of energy and width values for $(2s^2 2p)^2P$ and $(2s2p^2)^2D$ resonances

The current measurements agree well with most previous experimental and theoretical data as listed in Tables 2 and 3. In particular there is good agreement with the most recent experimental work of Trantham et al. [40] who have measured the $(2s^2 2p)^2P$ and $(2s2p^2)^2D$ resonances at 16º, 54º and 90º. Their results are shown together with the current results at those angles in Figures 3, 4 and 5 respectively.

In terms of other results and data listed in Tables 2 and 3, the resonant energies of the current measurements agree with all previous experimental data within errors. They are in agreement with all theoretical predictions apart from Nicolaides [29] and Nesbet [35] for the $(2s2p^2)^2D$ resonance, and Bylicki [38] and Bylicki and Nicolaides [39] for the $(2s^2 2p)^2P$ resonance. The resonant width measurements agree with Bylicki [38] at both energies and Gosselin [37] for the $(2s2p^2)^2D$ resonance, but not Smith [33] whose widths appear extremely small. Gosselin [37] and Quéméner [28] both agree well with the current measurements.

At 16º there are some small differences between the current work and Trantham et al. [40]. Background variation across the energy range in the current measurements meant the relatively strong decay of the $(2s^2 2p)^2P$ resonance to the 2^1P channel, which is seen in both the current work and Trantham et al. (see Figure 4), remains unresolved. A small resonance profile in the 2^3P channel for the $(2s2p^2)^2D$ resonance in the measurements of Trantham et al. [40] is absent in the current work, though a similar structure in the 2^1P channel is present in both sets of measurements. Apart from these differences in the 1s2p levels the remaining profiles were generally in very good agreement, with line shapes being only marginally different.

At 54º there is very good agreement with Trantham et al. [40]. The only significant difference between the data is the inability to resolve a possible $(2s2p^2)^2D$ resonance in the 2^1P channel which Trantham et al. [40] suggests may be present. For the remaining resonances the shape and tails agree, providing confidence in the accuracy of the results. The angular distribution of d-wave electrons emitted by the $(2s2p^2)^2D$ to $2^{1,3}S$ decays should vanish at 54º, as indicated above, and it is clear from the present data that it does.

At 90º there is generally good agreement between the results. Two resonance structures are resolved in the current work, which angular momentum considerations suggest should be absent, namely a $(2s2p^2)^2D$ resonance in the 2^1P channel, a $(2s^2 2p)^2P$ resonance in the 2^1S

channel. As can be seen from Figure 6 the $(2s2p^2)^2D$ resonance in the 2^1P channel appears to be the result of background fluctuations, whilst the spurious $(2s^22p)^2P$ resonance in the 2^1S channel is present in both the present work and that of Trantham et al. [40], suggesting that it may not be fictitious after all, and that some transitions to the 2^1S state occur at this energy, though it is not clear why this should occur. The $(2s2p^2)^2D$ resonance in the 2^1S channel could not be resolved despite being clearly visible in Figure 6. The earlier work of Chung and Davis [43] using a saddle-point technique suggests that this resonance doesn't exist with a He $(2s2p)^3\ P^o$ core being repulsive to a 2p electron and that the observed features could be as a result of a Post-Collision Interaction effect. Batelaan et al. [41] have also previously highlighted the issues with the proximity of the $(2s2p)^3P$ state to the ^2D resonance but it is unclear why this would be an issue within this decay channel. Figure 7 presents the present CCC results for the singlet channel resonances together with the corresponding experimental results. As can be seen from the theoretical results, the $(2s2p^2)^2D$ resonance in the 2^1P channel does show a resonance structure, though this is absent in the experimental results, whilst the $(2s^22p)^2P$ resonance is absent in the 2^1S channel in the theoretical results and present in the experimental results. The latest theoretical results agree well in both line shape and absolute values in the singlet states in Figure 7, but the complexity in modelling accurately in the autoionising range, together with significant variations in values in the triplet states, mean that a full comparison of theoretical and experimental line shapes will require further investigation.

5.2 Variations in resonance shapes for the $(2s^2 2p)^2P$ and $(2s2p^2)^2D$ resonances

Data for resonance decays to the four n=2 singly excited states at 0º and 180º are presented in figures 8 – 15. Fitted line shapes are shown as solid blue lines. Combining these results with data at the remaining angles studied enables the resonance behaviour across the angular range to be summarised.

In the 2^1P channel, the $(2s^2 2p)^2P$ resonance oscillates from an asymmetric shape with a low energy peak, to a symmetric peak, to an asymmetric shape with a high energy peak, to a symmetric dip, to an asymmetric shape with a low energy peak through the progression from 0º to 180º . This is the only channel in which the line shape is similar at 0º and 180º. The $(2s2p^2)^2D$ resonance is in general very weak in the 2^1P channel, and is only resolvable at 0º and 90º. At 0º it is a symmetric dip, and at 90º it is an asymmetric shape with a high energy peak.

In the 2^3P channel, the $(2s^2 2p)^2P$ resonance does not show the same line shape at 0º and 180º with the profile progressing from an asymmetric shape with a high energy peak, to a symmetric dip, to an asymmetric shape with a low energy peak, to a symmetric peak through the progression from 0º to 180º. Again the $(2s2p^2)^2D$ resonance is in general very weak in the 2^3P channel, and is only resolvable at 54º, where it is a symmetric dip, and at 90º where it is an asymmetric shape with a low energy peak.

In the 2^1S channel, the $(2s^2 2p)^2P$ resonance displays an unusual progression with angle in the 2^1S channel, though it is unclear why this should occur. It progresses from a symmetric dip, to an asymmetric shape with a low energy peak, to a symmetric peak, to a symmetric dip, to an asymmetric shape with a low energy peak, to a symmetric dip, to an asymmetric shape with a low energy peak through the progression from 0º to 180º. The $(2s2p^2)^2D$ resonance is far more pronounced in both the 1s2s channels. In the 2^1S channel the $(2s2p^2)^2D$ resonance progresses from an asymmetric shape with a low energy peak, to a symmetric dip, to an asymmetric shape with a low energy peak, to a symmetric dip, to an asymmetric shape with a high energy peak through the progression from 0º to 180º.

In the 2^3S channel, the $(2s^2 2p)^2P$ resonance progresses from an asymmetric shape with a high energy peak, to a symmetric peak through the progression from 0º to 180º. The $(2s2p^2)^2D$ resonance progresses from an asymmetric shape with a high energy peak, to a symmetric peak, to an asymmetric shape with a low energy peak through the progression from 0º to 180º.

5.3 Resonance cross sections for the $(2s^2 2p)^2P$ and $(2s2p^2)^2D$ resonances

As outlined in Equation 4, ρ^2 values give the ratio of resonant cross section to resonant plus non resonant cross section i.e. the proportion of electrons at a given energy and angle which have reached the final state via resonance. ρ^2 and resonant cross sections values are presented in Table 4 and Table 5 respectively. From the values calculated from the experimental data it is clear that in most circumstances very few electrons are involved in resonance behaviour. Of the 37 values stated in Table 4 only 8 values are above 10% and only 4 values above 50%.

The most striking feature is the almost pure resonant behaviour of electrons detected in the 2^3P channel at 54°. This channel also accounts for the entire decay from the $(2s2p^2)^2D$ resonance at this angle. Another significant feature is the 2^3S decay of the $(2s2p^2)^2D$ resonance at 180° where a large amount of the detected electrons have resonated.

At 90° the 2^1S decay from the $(2s2p^2)^2D$ resonance is given no value as it has proved impossible to fit the data, though the presence of a signal, as seen in Figure 6, implies that values for the resonant cross section, ρ^2, A and B, together with the resonant energy and width, would have been available if better resolution could have been achieved. This is also true for the 2^3P decay from the $(2s2p^2)^2D$ resonance at 180°.

An erroneous signal exists in the 2^1S decay channel for the $(2s^22p)^2P$ resonance at 90°. Its cause is unclear, but its presence in both the present and previous data suggests it may be due to another transition or interference between states. Further measurements with improved resolution are required to confirm this. The erroneous signal occurring in the 2^1P decay of the $(2s2p^2)^2D$ resonance at 90° has been discussed previously and has been attributed to background fluctuations.

The resonant cross sections at 54° and 90° provide valuable information on the arrangement of the electrons in the resonant structures. The propensity for the triplet decay channels at 54° in the 1s2p channel and at 90°in the 1s2s and 1s2p channels indicate resonant structures of the form $[2s(2s2p)^3P]^2P$ and $[2p(2s2p)^3P]^2D$ for the 57eV and 58eV resonances respectively. That is to say both negative ions are formed from a pair of correlated electrons external to an excited Coulomb core.

This result agrees with Trantham et al. [40] for the $(2s2p^2)^2D$ resonance but not the $(2s^22p)^2P$ resonance where Trantham et al. [40] suggest a $[2p(2s^2)^1S]^2P$ structure. The resonant decay of the $(2s2p^2)^2D$ to the 2^3P state at 54°, rather than the 2^1P state, indicates that the $(2s2p^2)^2D$ resonance highly favours detachment of the non-coupled p electron when decaying to the 1s2p level, a factor which would be difficult to reconcile if an alternative structure were correct.

6. Conclusions

The $2s^22p\ ^2P$ and $2s2p^2\ ^2D$ triply excited negative ion resonances in the autoionising region of helium have been measured for the first time over the complete angular range using a soft-core magnetic angle changer. The resonant structures for the triply excited negative ions are shown to be $[2s(2s2p)^3P]^2P$ and $[2p(2s2p)^3P]^2D$ for the 57eV and 58eV resonances respectively, with both negative ions formed from a pair of correlated electrons external to an excited Coulomb core. Initial developments have been made in theoretically modelling the 2^1S and 2^1P singlet channel resonance decays using the CCC theory, as shown in Figure 7, but significant challenges still remain. Unusual experimental behaviour has been observed for the $(2s^22p)^2P$ resonance in the 2^1S decay channel at 90°. This unusual behaviour may be as the result of a Post-Collision Interaction where this would not usually be expected, but current

modelling does not provide a clear explanation for this, and further investigation is therefore required.

Acknowledgments

The work of RW, DC, NB, GCK and FHR was supported by EPSRC grant GR/K90845/01, the work of DVF and IB was supported by the Australian Research Council, the Australian National Computing Infrastructure Facility and its Western Australian node Ivec.

Negative ion resonance measurements in the autoionising region of helium measured across the complete angular scattering range (0°-180°).

Tables

Negative ion states			Autoionising states		
Energy (eV)	Width (meV)	State	State	Energy (eV)	Width (meV)
			$2p^2\ ^1S$	62.13[d]	7
60.4[c,d]	1000	$2p^3\ ^2P$			
			$2s2p\ ^1P^o$	60.12[d]	44
			$2p^2\ ^1D$	59.87[a]	
59.71[a]	79	$2s2p^2\ ^2P$			
59.46[a]	282	$2p^3\ ^2D^o$			
59.4[b]	300	$2s2p^2\ ^2S$			
59.33[a]	bound	$2p^3\ ^4S^o$			
			$2s2p\ ^3P^o$	58.309[a]	8
58.303[e]	**49**	**$2s2p^2\ ^2D$**			
			$2s^2\ ^1S$	57.9[d]	130
57.42[a]	15	$2s2p^2\ ^4P$			
57.205[e]	**90**	**$2s^22p\ ^2P$**			

Table 1 - Energy scale for negative ion and doubly excited states (a - Nicolaides et al. [49]; b - Ormonde [50]; c - Nesbet [35]; d - Christophorou [51]); e - Bylicki and Nicolaides [39]. The negative ion resonances at 57.205eV and 58.303eV are shown in bold.

Paper	Method	Energy (eV)	Width (meV)
Kuyatt et al. [23]	Experimental	57.1 ± 0.1	
Grissom et al. [25]	Experimental	57.21 ± 0.06	
Quéméner [28]	Experimental	57.15 ± 0.04	90 ± 14
Sanche and Schulz [30]	Experimental	57.16 ± 0.05	
Marchand and Cardinal [31]	Experimental	57.2 ± 0.05	90 ± 200
Hicks et al. [34]	Experimental	57.22 ± 0.04	
Roy et al. [36]	Experimental	57.19 ± 0.03	
Nicolaides [29]	State Specific	57.3	
Smith [33]	Close Coupling	56.48	2.4
Ahmed and Lipsky [32]	Truncated diagonalisation	57.35	
Nesbet [35]	Stabilization	57.41	
Bylicki [38]	Feshbach projection	57.196	
Bylicki and Nicolaides [39]	Complex-coordinate rotation	57.205	71

Table 2 - Previous energy and width values for $(2s^22p)^2P$ resonance.

Paper	Method	Energy (eV)	Width (meV)
Kuyatt et al. [23]	Experimental	58.2 ± 0.1	
Grissom et al. [25]	Experimental	58.31 ± 0.08	
Quéméner [28]	Experimental	58.23 ± 0.04	50 ± 20
Sanche and Schulz [30]	Experimental	58.25 ± 0.05	
Marchand and Cardinal	Experimental	58.3 ± 0.05	

Negative ion resonance measurements in the autoionising region of helium measured across the complete angular scattering range (0°-180°).

[31]			
Hicks et al. [34]	Experimental	58.30 ± 0.04	
Roy et al. [36]	Experimental	58.29 ± 0.03	
Gosselin and Marmet [37]	Experimental	58.283 ± 0.003	59 ± 4
Nicolaides [41]	State Specific	58.4	
Smith et al. [33]	Close Coupling	58.34	24.6
Nesbet [35]	Stabilization	58.52	
Bylicki and Nicolaides [39]	Complex-coordinate rotation	58.303	49

Table 3 – Previously published energy and width values for $(2s2p^2)^2D$ resonance.

	2^3S		2^1S		2^3P		2^1P	
Degrees	$(2s^22p)^2P$	$(2s2p^2)^2D$	$(2s^22p)^2P$	$(2s2p^2)^2D$	$(2s^22p)^2P$	$(2s2p^2)^2D$	$(2s^22p)^2P$	$(2s2p^2)^2D$
0	0.015	0.038	0.004	0	0.006	-	0	0.024
18	0.03	0.05	0	0.003	0.007	-	-	-
54	0.012	-	0.16	-	0.994	0.999	0.087	-
90	-	0.023	0.003	-	0.613	-	0.029	0.013
108	-	0.012	-	-	0.158	-	0.176	-
126	0.016	0	0	0.005	0.049	-	0.041	-
180	0.133	0.837	0.002	0.001	0.013	-	0.017	-

Table 4 - ρ^2 values for $(2s^22p)^2P$ and $(2s2p^2)^2D$ resonances at various angles.

	2^3S		2^1S		2^3P		2^1P	
Degrees	$(2s^22p)^2P$	$(2s2p^2)^2D$	$(2s^22p)^2P$	$(2s2p^2)^2D$	$(2s^22p)^2P$	$(2s2p^2)^2D$	$(2s^22p)^2P$	$(2s2p^2)^2D$
0	7.76	19.7	3.47	0.42	0.025	-	0.013	1.57
18	4.77	5.65	0.357	3.35	0.05	-	-	-
54	0.217	-	21.3	-	1.22	6.55	0.034	-
90	-	0.025	0.123	-	0.052	-	0.026	0.011
108	-	0.005	-	-	0.055	-	0.163	-
126	0.007	0	0.006	0.124	0.047	-	0.04	-
180	0.043	1.04	0.041	0.049	0.024	-	0.02	-

Table 5 - Resonance cross sections for $(2s^22p)^2P$ and $(2s2p^2)^2D$ resonances at various angles in units of $10^{-19}cm^2/sr$.

Negative ion resonance measurements in the autoionising region of helium measured across the complete angular scattering range (0°-180°).

Figures

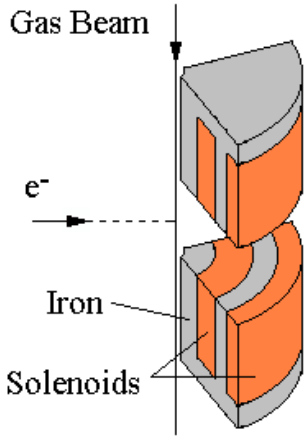

Figure 1 - A quarter cross section of iron-cored coil system. The total radius of the coil is 15 mm and the length of one coil is approximately 12 mm. The positions of the iron cores are shown at the top of the diagram in grey.

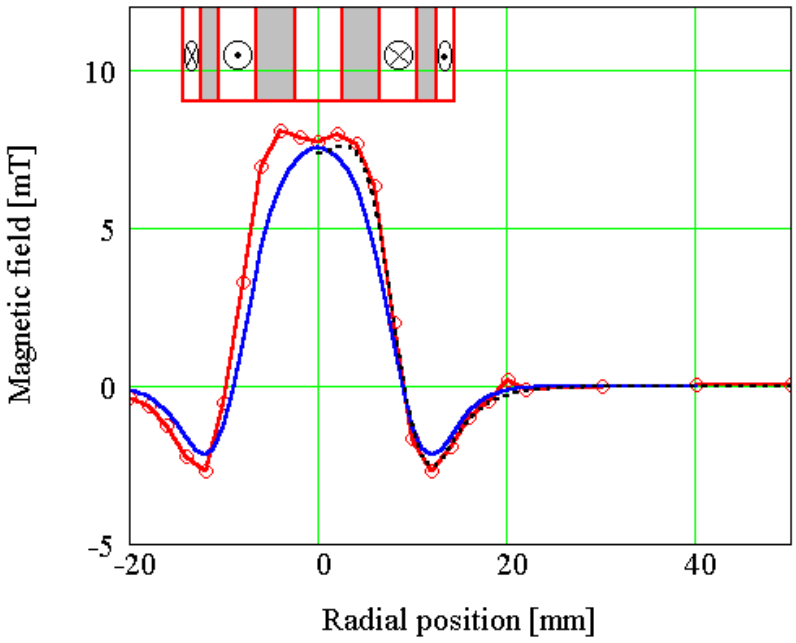

Figure 2 - The circles indicate magnetic field measurements for the complete coil system. The dotted line represents the calculated fields for the coil using Equation 6.The smooth curve without circles represents the magnetic field variation for a MAC without an iron core, scaled up by a factor of 5.

Negative ion resonance measurements in the autoionising region of helium measured across the complete angular scattering range (0°-180°).

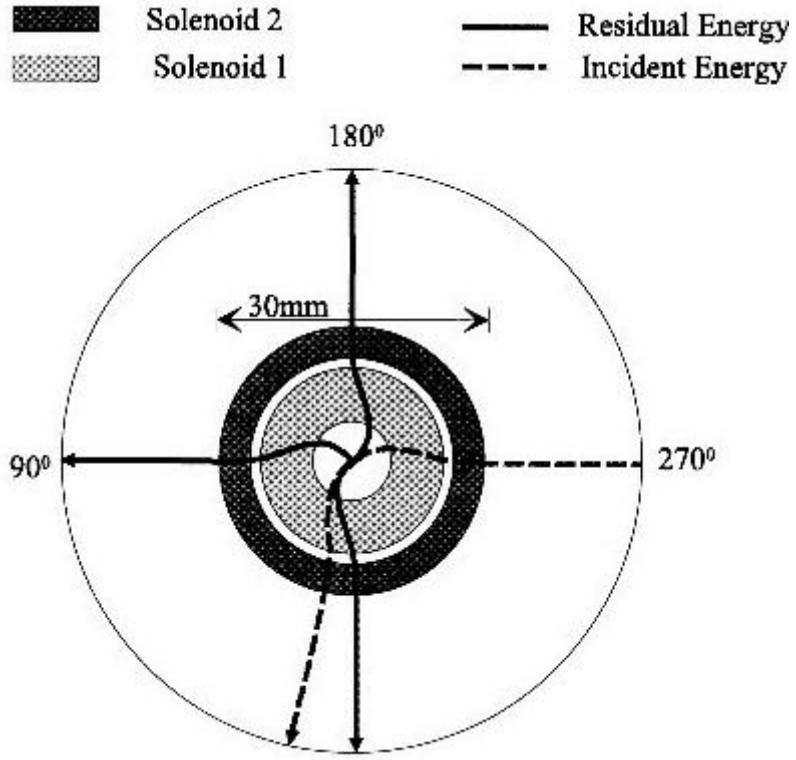

Figure 3 - Motion of electrons under the influence of the Magnetic Angle Changer for nominal incident and residual energies of 40eV and 20eV respectively.

Negative ion resonance measurements in the autoionising region of helium measured across the complete angular scattering range (0°-180°).

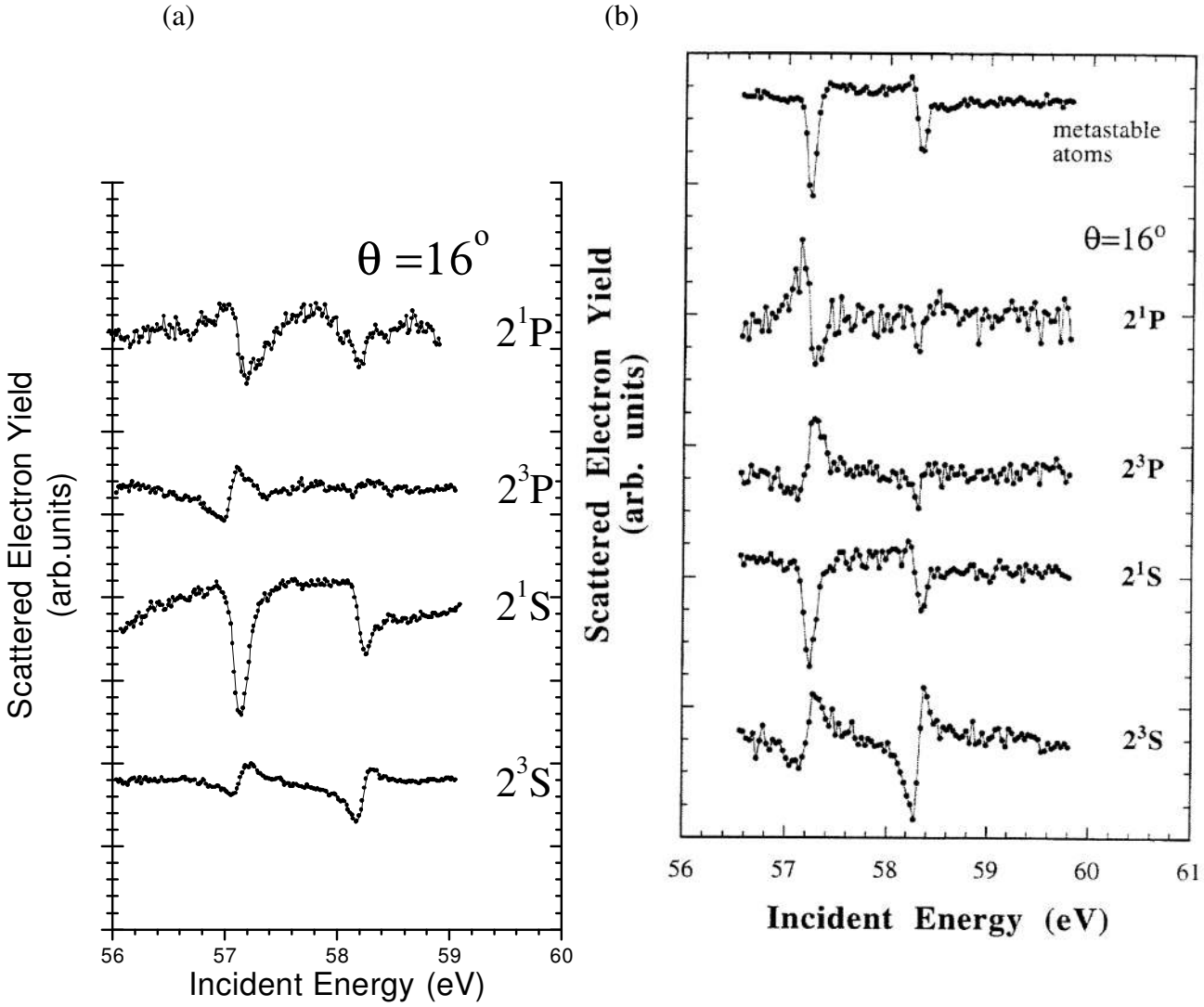

Figure 4 - Comparison of (a) excitation functions obtained in the current work with (b) those of Trantham et al. [40] at 16º, presented side-by-side to highlight similarities.

Negative ion resonance measurements in the autoionising region of helium measured across the complete angular scattering range (0°-180°).

(a) (b)

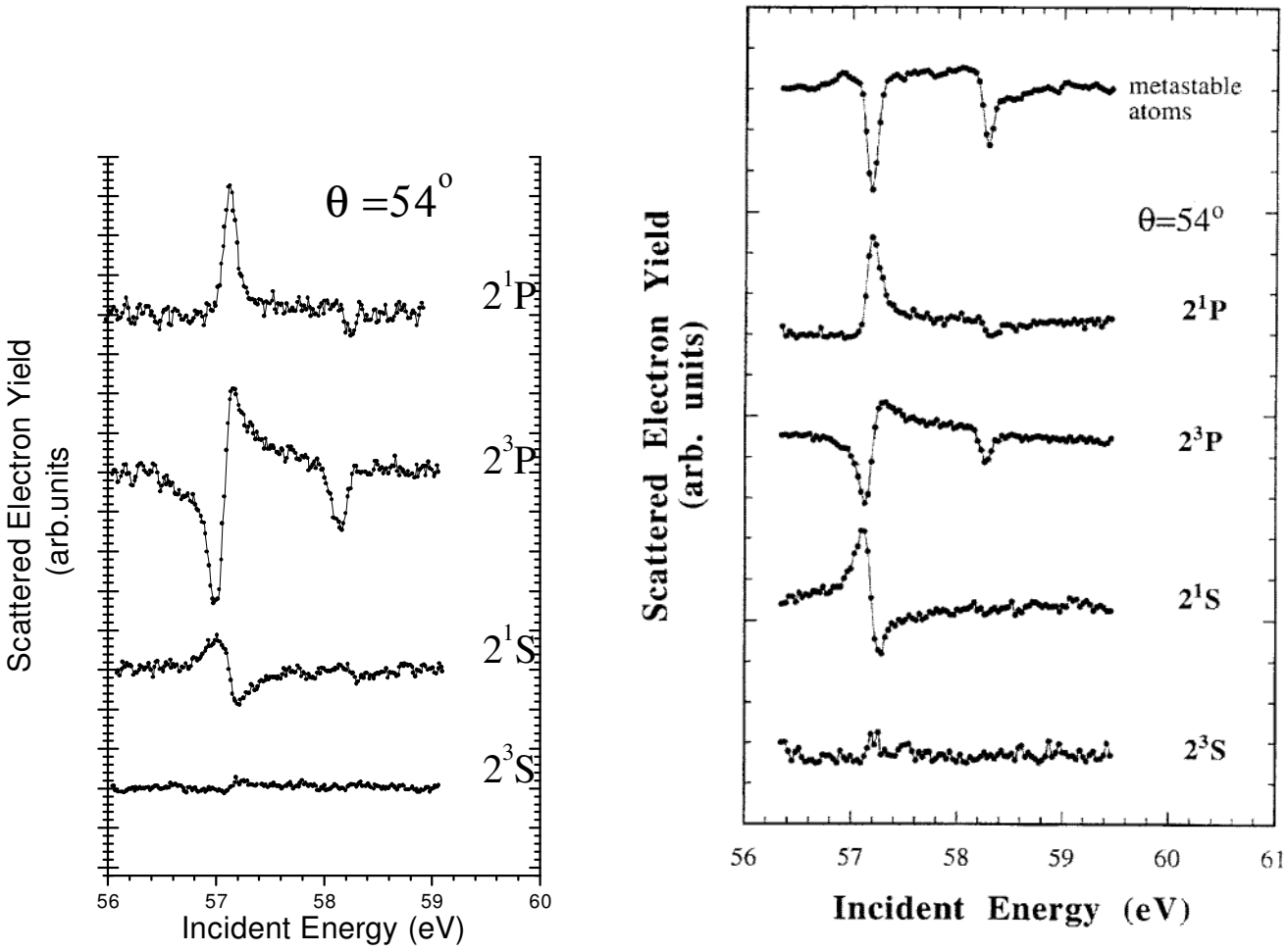

Figure 5 – Comparison of (a) excitation functions obtained in the current work with (b) those of Trantham et al. [40] at 54º, presented side-by-side to highlight similarities.

Negative ion resonance measurements in the autoionising region of helium measured across the complete angular scattering range (0°-180°).

(a) (b)

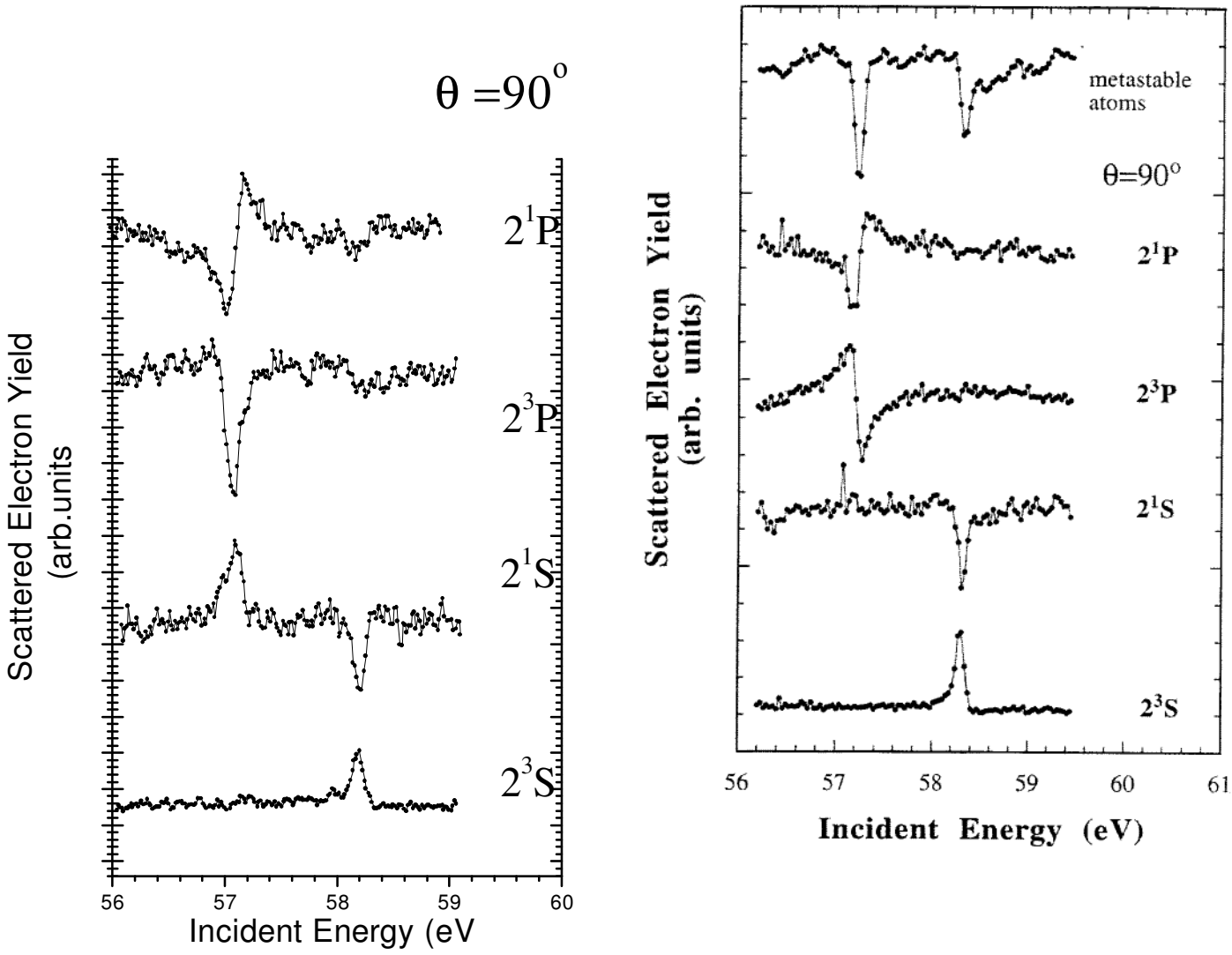

Figure 6 – Comparison of (a) excitation functions obtained in the current work with (b) those of Trantham et al. [40] at 90º, presented side-by-side to highlight similarities.

Negative ion resonance measurements in the autoionising region of helium measured across the complete angular scattering range (0°-180°).

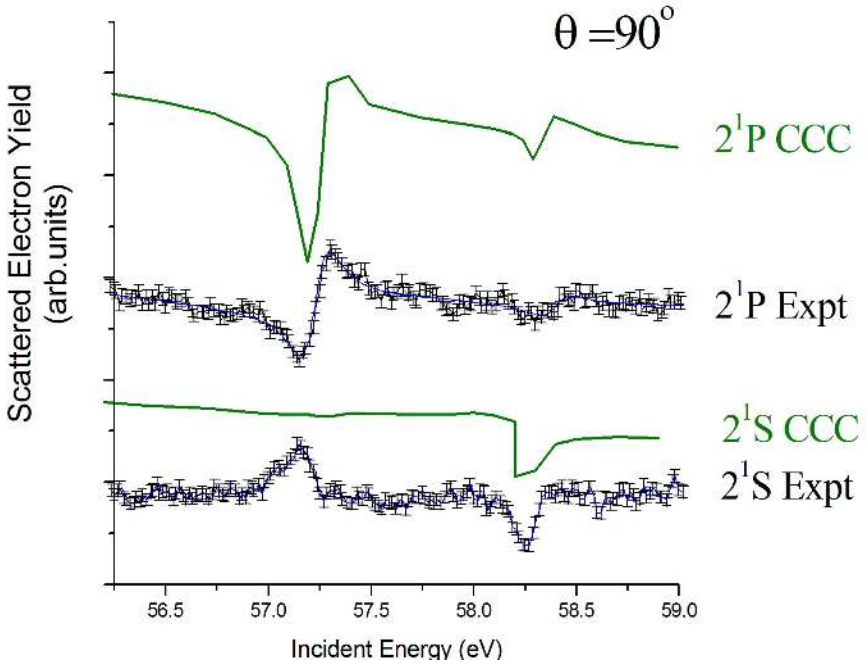

Figure 7 - Comparison of theoretical and experimental line shapes for the contested resonance features at 90º in the singlet decay channels. The results are separated vertically to enable clear comparison of the line shapes.

Negative ion resonance measurements in the autoionising region of helium measured across the complete angular scattering range (0°-180°).

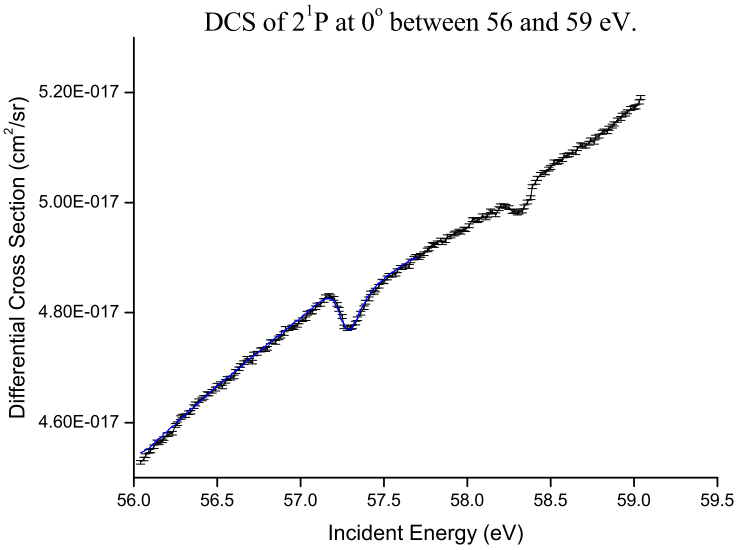

Figure 8 - $(2s^2 2p)^2P$ and $(2s2p^2)^2D$ resonances in the 2^1P channel at 0º

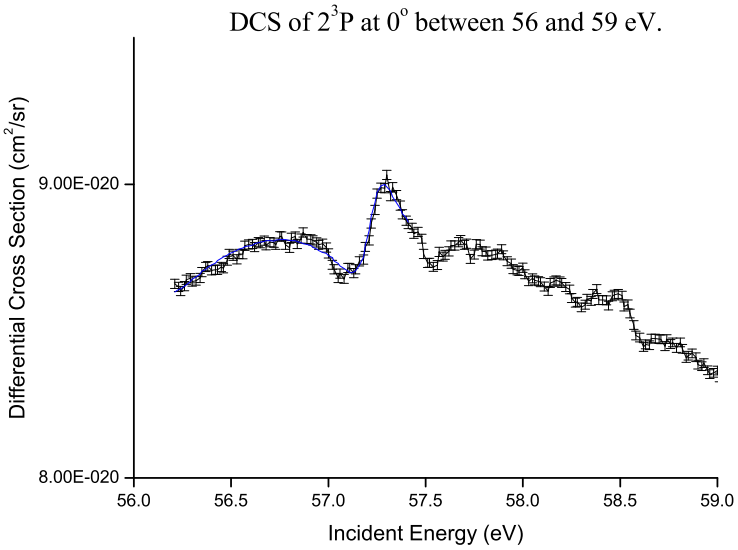

Figure 9 - $(2s^2 2p)^2P$ and $(2s2p^2)^2D$ resonances in the 2^3P channel at 0º

Negative ion resonance measurements in the autoionising region of helium measured across the complete angular scattering range (0°-180°).

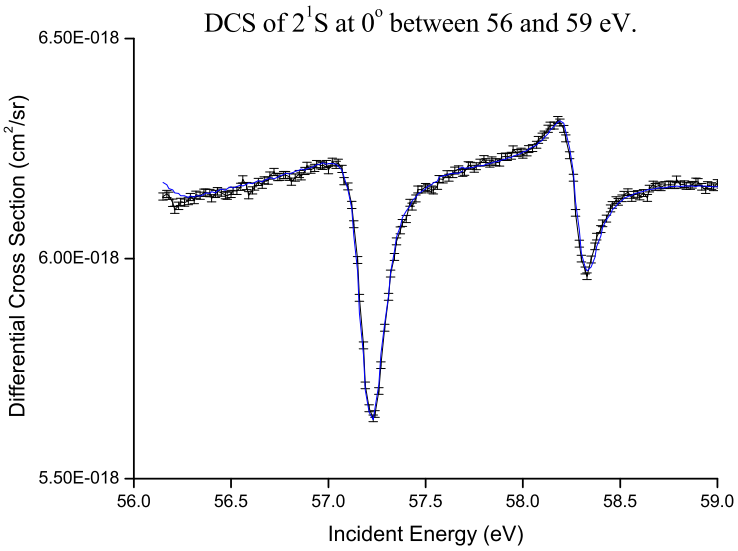

Figure 10 - $(2s^2 2p)^2P$ and $(2s2p^2)^2D$ resonances in the 2^1S channel at 0º

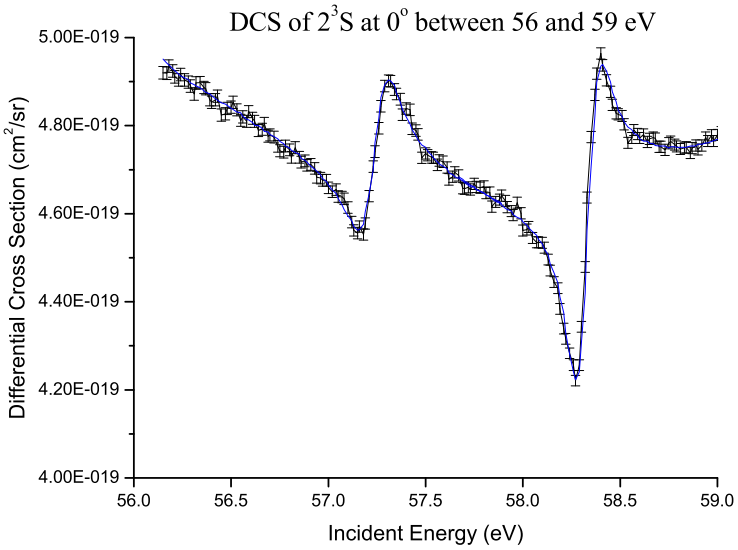

Figure 11 - $(2s^2 2p)^2P$ and $(2s2p^2)^2D$ resonances in the 2^3S channel at 0º

Negative ion resonance measurements in the autoionising region of helium measured across the complete angular scattering range (0°-180°).

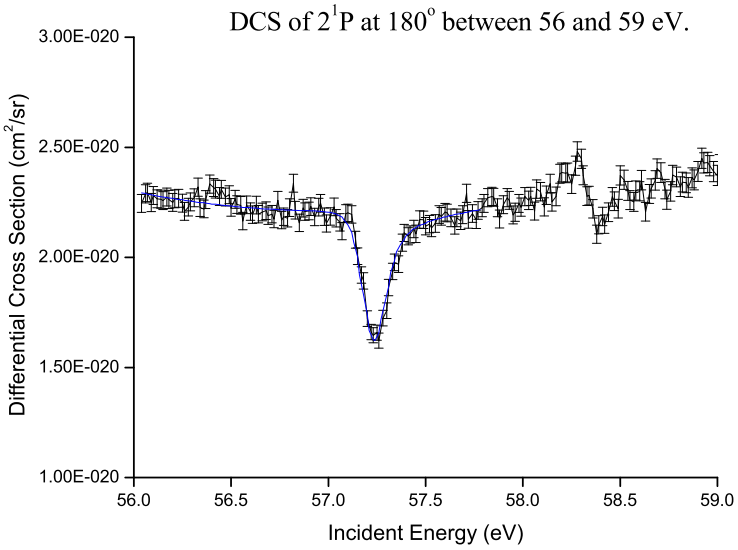

Figure 12 - $(2s^2 2p)^2P$ and $(2s2p^2)^2D$ resonances in the 2^1P channel at 180º

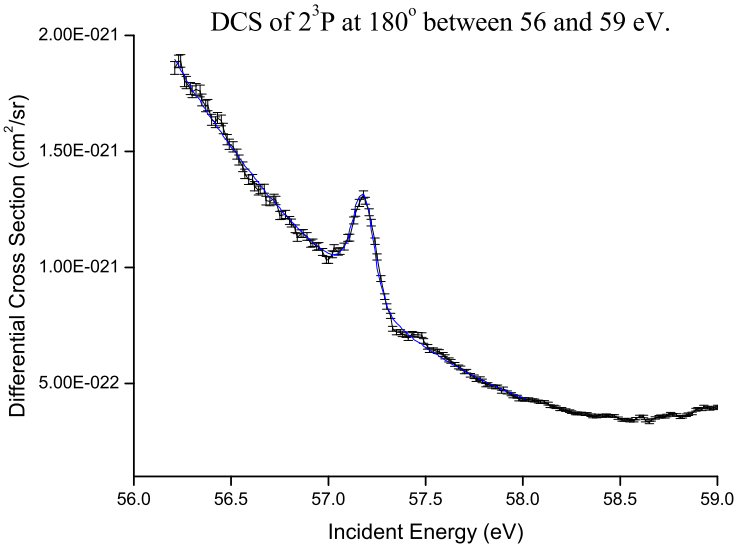

Figure 13 - $(2s^2 2p)^2P$ and $(2s2p^2)^2D$ resonances in the 2^3P channel at 180º

Negative ion resonance measurements in the autoionising region of helium measured across the complete angular scattering range (0°-180°).

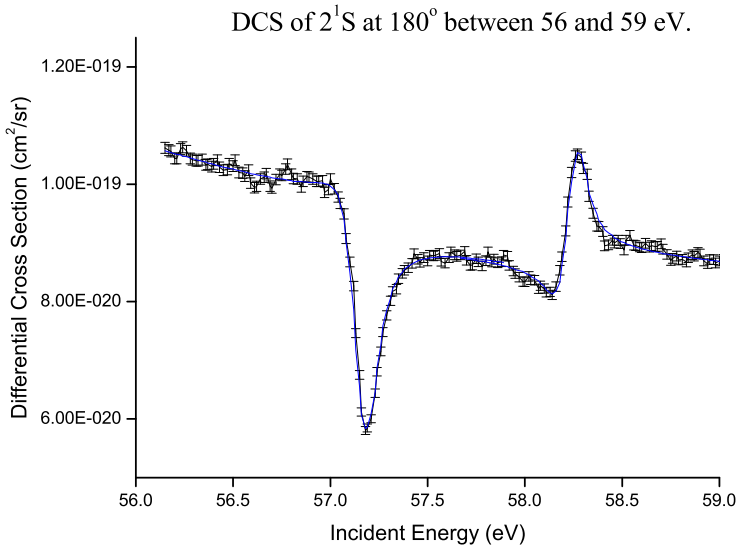

Figure 14 - $(2s^2 2p)^2P$ and $(2s2p^2)^2D$ resonances in the 2^1S channel at 180º

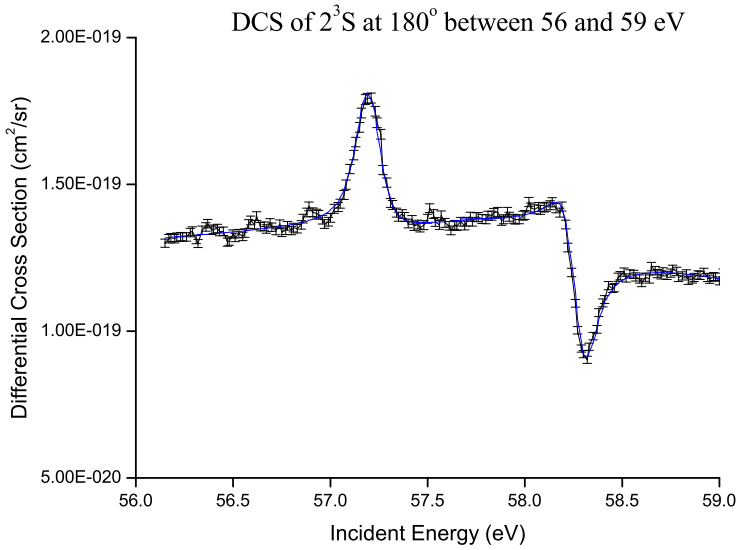

Figure 15 - $(2s^2 2p)^2P$ and $(2s2p^2)^2D$ resonances in the 2^3S channel at 180º

[1] Schulz G. J. (1963), *Phys. Rev. Lett.*, 10, 3, 104
[2] Qazilbash, M. M., Hamlin, J. J., Baumbach, R. E., Zhang, L., Singh, D. J., Maple, M. B. and Basov, D. N. (2009) *Nature Phys.*, 5, 647
[3] Yamaguchi, K., Yamaki, D., Kitagawa, Y., Takahata, M., Kawakami, T., Ohsaku, T. and Nagao, H. (2003) *Int. J. Quantum Chem.*, 92, 47-70
[4] Neto, A. H. C., Guinea, F. , Peres, N. M. R., Novoselov, K. S., and Geim, A. K. (2009) *Rev. Mod. Phys.*, 81, 109
[5] Oohara, W., Date, D. and Hatakeyama, R. (2004) arXiv:physics/0410167
[6] Tans, S. J., Devoret, M. H., Groeneveld, R. J. A. and Dekker, C. (1998) *Nature*, 394, 6695, 761-764
[7] Yuen, J. D., Menon, R., Coates, N. E., Namdas, E. B., Cho, S., Hannahs, S. T., Moses, D. and Heeger, A. J. (2009) *Nat. Mater.*, 8,7, 572
[8] Treumann, R. A., Klos, Z. and Parrot, M. (2008) *Space Sci. Rev.*, 137, 133-148
[9] Larsson, M., Geppert, W. D. and Nyman, G. (2012) *Rep. Prog. Phys.*, 75, 066901
[10] Grant Hill, J., Platts, J. A. and Werner, H-J. (2006) *Phys. Chem. Chem. Phys.*, 8, 35, 4072-4078
[11] Zhou H. L., Manson S. T., Vo Ky L., Hibbert, A. and Feautrier, N. (2001) *Phys. Rev. A*, 64, 012714
[12] Piangos, N. A. and Nicolaides, C. A. (2001) *J. Phys. B : At. Mol. Opt. Phys.*, 34, L633–L643
[13] Fursa, D. V. and Bray, I. (1995) *Phys. Rev. A*, 52, 2, 1279-97
[14] Fano U. (1961) *Phys. Rev.*, 124, 6, 1866-78
[15] Fano U. and Cooper J. W. (1965) *Phys. Rev. A*, 137, 5A, 1364-79
[16] Schulz G. J. (1973) *Resonances in Electron Impact on Atoms*, Rev. Mod. Phys., 45, 378
[17] Buckman S. J. and Clark C. W. (1994) *Atomic negative-ion resonances*, Rev. Mod. Phys., 66, 539
[18] Taylor, H. S., Nazaroff, G. V. and Golebiewski, A. (1966) *J. Chem. Phys.*, 45, 2872
[19] Taylor H. S. (1970) *Adv. Chem. Phys.*, 18, 91
[20] Simpson, J. A., Menendez, M. G. and Mielczarek, S. R. (1966) *Phys. Rev.*, 150, 76
[21] Shore B. W. (1967) *Rev. Mod. Phys.*, 39, 439
[22] Comer J. and Read F. H. (1972) *J. Phys. E*, 5, 211
[23] Kuyatt C. E., Simpson, J. A. and Mielzyarek, S. R. (1965) *Phys. Rev. A*, 138, 2, 385
[24] Burrow, P.D. and Schulz, G.J. (1969) *Phys. Rev. Lett.*, 22,1271
[25] Grissom J. T., Compton, R.N. and Garrett, W.R. (1969) *Phys. Lett.*, 30A, 117
[26] Eliezer, I. and Pan, Y. K. (1970) *Theoret. Chim. Acta*, 16, 63
[27] Golden, D. E. and Zecca, A. (1970) *Phys. Rev. A*, 1, 241-249
[28] Quéméner J. J. (1971) *Phys. Rev. A*, 4, 494
[29] Nicolaides C. A. (1972) *Phys. Rev. A*, 6, 2078
[30] Sanche L. and Schulz G. J. (1972) *Phys. Rev. A*, 5, 1672-83
[31] Marchand P. and Cardinal J. (1973) *Can. J. Phys.*, 51, 814
[32] Ahmed A and Lipsky L. (1975) *Phys. Rev. A*, 12, 1176-96
[33] Smith K., Golden, D.E., Ormonde, S., Torres, B. and Davies, A. R. (1973) *Phys. Rev. A*, 8, 6, 3001-11
[34] Smith, A. J., Hicks, P. J., Read, F. H., Cvejanović, S., King, G. C. M., Comer, J. and Sharp, J. M. (1974) *J. Phys. B : At. Mol. Opt. Phys.*, 7, L496-501
[35] Nesbet, R. K. (1976) *Phys. Rev. A*, 14, 4, 1326-32
[36] Roy D., Delage A. and Carette J. D. (1978) *J. Phys. B : At. Mol. Opt. Phys.*, 11, 23, 4059
[37] Gosselin, R. N. and Marmet, P. (1990) *Phys. Rev. A*, 41, 1335-9
[38] Bylicki, M. (1992) *Phys. Rev. A*, 45, 2079-82
[39] Bylicki, M. and Nicolaides, C. A. (1995) *Phys. Rev. A*, 51, 1, 204-10
[40] Trantham K. W., Jacka, M., Rau, A. R. P. and Buckman, S. J. (1999) *J. Phys. B : At. Mol. Opt. Phys.,* 32, 815-824
[41] Batelaan, H., Van Eck, J. and Heideman, H. G. M. (1991) *J. Phys. B : At. Mol. Opt. Phys.*, 24, 5151-5167
[42] Nicolaides, C. A. and Piangos, N. A. (2001) *Phys. Rev. A*, 64, 052505–17

[43] Chung, K. T. and Davis, B. F. (1985) in *Autoionisation*, edited by A Temkin (Plenum, New York) 73
[44] Morishita T. and Lin C. D. (1998) *J. Phys. B : At. Mol. Opt. Phys.*, 31, L209-17
[45] Read F H and Channing J M (1996) *Rev. Sci. Instrum.*, **67**, 2372-77
[46] Cubric, D., Thompson, D. B., Cooper, D. R., King, G. C. and Read, F. H. (1997) *J. Phys. B. At. Mol. Opt. Phys.* **30** L857
[47] Ward, R., Cubric, D., Bowring, N., King, G. C., Read, F. H., Fursa, D. V., Bray, I., Zatsarinny, O. and Bartschat, K. (2011) *J. Phys. B. At. Mol. Opt. Phys.***44** 045209
[48] Fursa, D. V. and Bray, I. (1997) *J. Phys. B : At. Mol. Opt. Phys.*, **30**, 757-85
[49] Nicolaides C. A., Piangos, N. A. and Komninos, Y. (1993) *Phys. Rev. A*, 48, 5, 3578
[50] Ormonde S., Kets, F. and Heidman, H. G. M. (1974) *Phys. Lett.*, 50A, 147-8
[51] Christophorou L. G. (1984) *Electron-molecule interactions and their applications* (Academic Press) 1, 477-617